Finite Element Modeling of Thermoelectric Effects in Phase Change Memory Cells

M. T. B. Kashem^a, J. Scoggin^{a,b}, H. Silva^a and A. Gokirmak^a

We model the current density in a semiconductor based on the drift-diffusion transport of the charge carriers to accurately determine the thermoelectric effects in the bulk material (Thomson effect) and material junctions (Peltier effect). We utilize the model to perform 2-D finite element simulations of mushroom phase change memory cell with a critical dimension of 20 nm using temperature and electric field dependent material parameters and analyze the contributions of symmetric Joule heating and asymmetric thermoelectric heats during reset and set operations. We investigate the effect of altering the direction of current flow by changing the connection point between the cell and the access device and observe that, corresponding change in thermoelectric effects cause significant difference in operation dynamics, temperature distribution profiles, amorphous volume, energy requirement and resistance contrast between reset and set states.

Introduction

Phase change memory (PCM) is an emerging non-volatile electronic memory technology which offers fast read/write times, high endurance to repeated cycling, long data retention, low voltage operation and high scalability to smaller dimensions (1-4). PCM utilizes the electrical resistivity difference between the amorphous and crystalline phases of phase change materials to store information. A typical PCM cell consists of a phase change material, typically a chalcogenide such as Ge₂Sb₂Te₅ (GST), sandwiched between two contacts. Short duration electrical current pulses are utilized to self-heat the cells in order to switch the cell from crystalline to amorphous phase by melting and sudden quenching (reset) or to self-heat above glass transition temperature (T_{glass}) to crystallize (set). During this fast and reversible switching, the cells experience extremely large thermal gradients (~ 50 K/nm) and high current densities (~ 50 MA/cm²) which result in significant coupling between heat current and electrical current. Therefore, thermoelectric (TE) effect induced heating or cooling contributions in the bulk and at materials and solid-liquid interfaces become very significant during the device operation (5-8). The direction of current flow determines the locations of heat release (heating) or absorption (cooling) due to TE effects and thereby impacts the energy requirements for reset-set operations (9). With proper selection of the phase change and contact materials and operation voltage pulse polarity, TE effects can be utilized to reduce the power consumption and enable ultralow power nanoscale device operation (5, 10, 11).

^a Department of Electrical and Computer Engineering, University of Connecticut, Storrs, Connecticut 06269, USA

^b Department of Computer Science and Engineering, University of Connecticut, Storrs, Connecticut 06269, USA

Previously, we have performed finite element analysis of the reset operation on mushroom PCM cell in COMSOL Multiphysics (12) to analyze TE effects (5). There we utilized effective media approximation to model the crystallization and amorphization dynamics which is useful to simulate large scale PCM devices (13). Later, we developed the model to capture discrete nucleation and growth of individual grains while tracking crystal orientation and grain boundaries (14), ensure energy conservation in amorphization-crystallization cycles by coupling the latent heat of phase change with specific heat (15) and implement heterogeneous melting to model the initiation of melting at the high energy sites; grain boundaries and material interfaces (16). In the present work, we use our latest model (16) to perform 2-D finite element electro-thermal simulations of 20 nm mushroom PCM cells in order to investigate the effects of thermoelectrics and the direction of current flow through the cell on the melting, amorphization and recrystallization of GST during reset and set operations. We employ a precise charge transport model formulated considering the drift-diffusion of the carriers and using the thermoelectric characteristics of the material. Besides, we utilize electric field and temperature dependent material parameters (15,17) to accurately capture the strong coupling between charge and heat transport in PCM.

Device Structure

Typical PCM mushroom cells share a top contact and are individually addressed through their bottom contact. The simulated geometry in this computational study consists of GST as the phase change material with width, W = 180 nm and height, h = 50 nm, a narrow (W = 20 nm) TiN bottom electrode known as heater, a TiN top electrode and SiO_2 used to isolate the neighboring cells (Figure 1). Three TiN heaters, separated by 30 nm, represent three PCM cells sharing the same GST region and top electrode. An n-channel metal oxide semiconductor field effect transistor (MOSFET) is used as an access device. A voltage pulse is applied to the gate of the MOSFET to control the reset, set and read operations. The connection of the MOSFET defines the positive and negative polarity configurations.

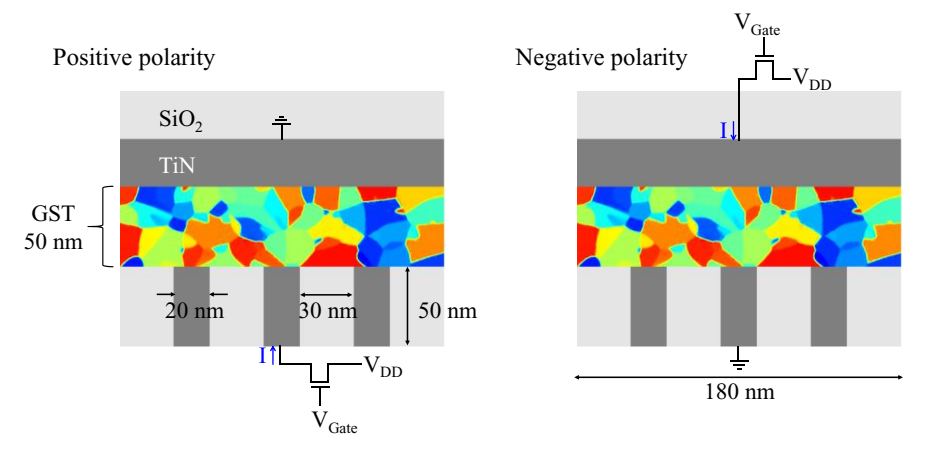


Figure 1. Planar PCM mushroom cell geometry and materials simulated in COMSOL Multiphysics. TiN is used as the top and bottom electrodes, GST is the phase change material and SiO₂ acts as an insulator to isolate the neighbor cells. The connection of the n-channel MOSFET defines the positive and negative polarity configurations. GST is shown as polycrystalline material with different color representing different crystal orientation of the grains.

Physics Model

In the simulation framework, we solve the heat transport and current continuity equations [equation (1) and (2) respectively] self-consistently using electric current and heat transfer physics and utilize our PCM physics model (13-16) to obtain the potential, temperature and phase changes in the device structure.

$$\underline{dC_p \frac{dT}{dt}} - \underline{V.(k\nabla T)} = -\underline{VV.J} - \underline{V.(JST)} + \underline{Q_H}$$
Heat absorbed Fourier heat Joule Thermo- Latent heat of by the material conduction heat electric heat phase change

$$\nabla J = -\frac{\partial \rho_v}{\partial t}$$
 [2]

where d is the mass density, C_p is the specific heat, T is the temperature, t is the time, k is the thermal conductivity, V is the electric potential, J is the electric current density, S is the Seebeck coefficient, Q_H represents the latent heat of phase change, and ρ_v is the volume charge density. In earlier works (5,8,16,18), the following more common form of J was used,

$$J = -\sigma \nabla V - \sigma S \nabla T \tag{3}$$

where σ is the electrical conductivity. Here the first term in the right side $(-\sigma \nabla V)$ is the drift current density component due to the applied electric field and the second term $(-\sigma S \nabla T)$ is the diffusion current component for a uniform material where only temperature gradient results in diffusion of charge carriers (19) and does not capture current driven by carrier concentration and Seebeck gradients. However, large thermal gradient (~50 K/nm)

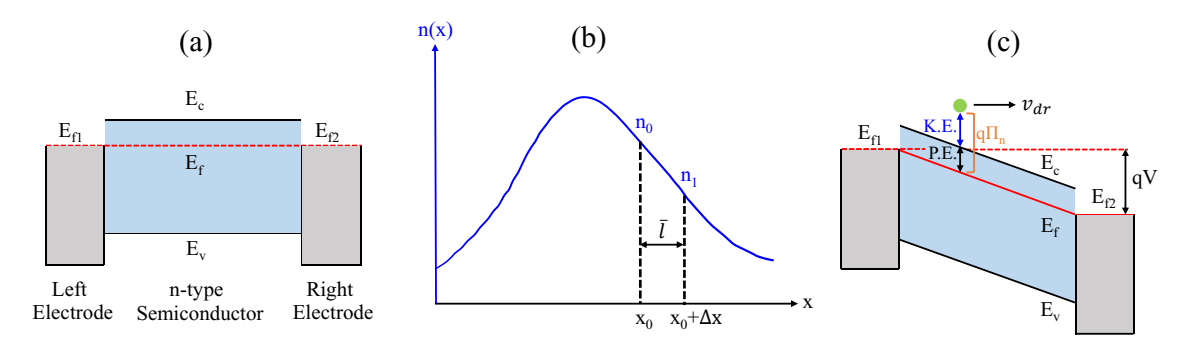


Figure 2. (a) Schematic energy band diagram of an n-type semiconductor with contacts at two ends in equilibrium. (b) Carrier concentration, n versus position, x in the semiconductor; n_0 and n_1 are the concentrations at x_0 and $x_0+\Delta x$ respectively, \bar{l} is the mean free path. (c) Energy band diagram of the same device in (a) under an external bias voltage, V causing a split of the Fermi level of the two metal contacts, $E_{f1} - E_{f2} = qV$. Solid red line indicates the change of the Fermi level inside the semiconductor, green circle represents an electron and the arrow next to it shows drift velocity (v_{dr}) due to the applied electric field. K.E. is the kinetic energy $(\frac{3}{2}k_BT)$ where k_B is the Boltzmann constant and P.E. is the chemical potential energy (E_c-E_f) of the electron. Peltier coefficient, $\Pi_n = \frac{1}{-q} \left[\frac{3}{2}kT + (E_c - E_f)\right]$

and high current densities (~50 MA/cm²) in PCM give rise to significant gradients in carrier concentrations and Seebeck coefficients. Therefore, along with temperature gradient, gradients of conductivity and Seebeck coefficient play significant role in PCM device operation and need to be incorporated in equation (3).

In this work, we derive an updated model of J for cases of significant thermal gradients following the procedure detailed in (20). We start by assuming an n-type semiconductor bar having arbitrary carrier concentration throughout with two contacts at the two ends (Figure 2a,b). Here $n_0 = n(x_0)$ is the concentration at x_0 while $n_1 = n(x_0 + \Delta x)$ is the concentration at $x_0 + \Delta x$. Electrons move from left to right when an external voltage, V is applied to the right contact (Figure 2c). Carrier velocity consists of drift velocity (v_{dr}) and thermal velocity (v_{th}) . Due to the random nature of thermal motion, there is equal probability for electrons to move to the right and left from their current positions which corresponds to different magnitude and direction of v_{th} . For instance, at a particular time, $\frac{n_0}{2}$ electrons will move to the right and $\frac{n_0}{2}$ electrons will move to the left from x_0 . At any position in between x_0 and $x_0 + \Delta x$, net electron flux density due to electrons moving from left to right (considering contributions of n_0 and n_1 only) is given by,

$$\Phi_{n}(x) = \frac{n_{0}}{2} v_{net}(x_{0}) - \frac{n_{1}}{2} v_{net}(x_{0} + \Delta x)$$

$$= \frac{1}{2} n(x_{0}) \{ v_{th}(x_{0}) + v_{dr}(x_{0}) \} - \frac{1}{2} n(x_{0} + \Delta x) \{ v_{th}(x_{0} + \Delta x) - v_{dr}(x_{0} + \Delta x) \}$$

$$= \frac{1}{2} \left[\frac{n(x_{0})v_{th}(x_{0}) - n(x_{0} + \Delta x)v_{th}(x_{0} + \Delta x)}{\Delta x} \right] \Delta x + \frac{1}{2} \left[n(x_{0})v_{dr}(x_{0}) + n(x_{0} + \Delta x)v_{dr}(x_{0} + \Delta x) \right]$$

$$= \frac{1}{2} \left[\frac{n(x_{0})v_{th}(x_{0}) - n(x_{0} + \Delta x)v_{th}(x_{0} + \Delta x)}{\Delta x} \right] \overline{l} + (nv_{dr})_{average}$$
[4]

where we assume Δx = mean free path = \bar{l} . For the limiting case of small Δx , equation (4) can be expressed as,

$$\Phi_n(x) = \frac{1}{2} \lim_{\Delta x \to 0} \left[\frac{n(x_0)v_{th}(x_0) - n(x_0 + \Delta x)v_{th}(x_0 + \Delta x)}{\Delta x} \right] \overline{l} + (nv_{dr})_{average}$$

$$= \frac{1}{2} \left\{ \frac{-d(nv_{th})}{dx} \right\} \overline{l} + (nv_{dr})_{average}$$
[5]

The current density for electrons, J_n is the product of the electron charge and flux density,

$$J_{n} = (-q)\Phi_{n}(x) = (-q)\left[\frac{1}{2}\left\{\frac{-d(nv_{th})}{dx}\right\}\overline{l} + (nv_{dr})\right]$$

$$= (-q)\frac{1}{2}\left\{\frac{-d\left(\frac{n\overline{l}^{2}}{\overline{t}}\right)}{dx}\right\} + (-q)n(-\mu_{n}E)$$
[6]

where $v_{th} = \frac{l}{\bar{t}}$, \bar{t} is the mean free time, and $v_{dr} = -\mu_n E$, μ_n is the electron mobility and E is the electric field. Equation (6) can then be re-written as,

$$J_n = \left\{ \frac{d\left(\frac{qn\overline{l}^2}{2\overline{t}}\right)}{dx} \right\} + qn\mu_n E = \frac{d(qnD_n)}{dx} + qn\mu_n E = J_{n,diffusion} + J_{n,drift}$$
 [7]

where $D_n = \frac{\overline{l}^2}{2\overline{t}}$ is the electron diffusion coefficient (20) and $J_{n,diffusion} = \frac{d(qnD_n)}{dx}$ and $J_{n,drift} = qn\mu_n E$ are the diffusion and drift components of the current density. $J_{n,drift}$ can be further modified to account for the thermoelectric effects through Peltier coefficient,

$$-q\Pi_n = -qS_nT = Kinet. Energy + Chem. Pot. Energy = \frac{3}{2}k_BT + (E_c - E_f)$$
 [8]

Here S_n is the Seebeck coefficient of electron, E_c is the conduction band edge, E_f is the Fermi energy level, $\frac{3}{2}k_BT$ is the kinetic energy where k_B is the Boltzmann constant and $E_c - E_f$ is the chemical potential energy of the electron.

Therefore,
$$E_c = (-q)\Pi_n - \frac{3}{2}k_BT + E_f$$
 [9]

Electrostatic force (F) experienced by the electron is,

$$F = (-q)E = -\frac{dE_c}{dx} = -\frac{d(-q\Pi_n - \frac{3}{2}k_BT + E_f)}{dx}$$

$$= q\frac{d\Pi_n}{dx} + \frac{3}{2}k_B\frac{dT}{dx} - \frac{dE_f}{dx} = q\frac{d\Pi_n}{dx} + \frac{3}{2}k_B\frac{dT}{dx} + q\frac{dV}{dx}$$
[10]

Using equation (10), $J_{n,drift}$ can be expressed as,

$$J_{n,drift} = n\mu_n(qE) = -n\mu_n \left[q \frac{d\Pi_n}{dx} + \frac{3}{2} k_B \frac{dT}{dx} + q \frac{dV}{dx} \right]$$

$$= -(qn\mu_n) \left[\frac{d\Pi_n}{dx} + \frac{3k_B}{2q} \frac{dT}{dx} + \frac{dV}{dx} \right] = -\sigma_n \frac{d(V + \Pi_n + \frac{3k_BT}{2q})}{dx}$$
[11]

where $\sigma_n = qn\mu_n$ is the electron component of conductivity. Using the Einstein relation, $D_n^{Einstein} = \mu_n \frac{k_B T}{q}$, $J_{n,diffusion}$ can be given by,

$$J_{n,diffusion} = \frac{d(qnD_n^{Einstein})}{dx} = \frac{d(\frac{qn\mu_n k_B T}{q})}{dx} = \frac{d(\frac{\sigma_n k_B T}{q})}{dx}$$
[12]

Combining equation (7), (11) and (12), J_n can be given by,

$$J_n = -\sigma_n \frac{d\left(V + \Pi_n + \frac{3k_B}{2q}T\right)}{dx} + \frac{d\left(\frac{\sigma_n k_B T}{q}\right)}{dx}$$
[13]

For the three-dimensional space, equation (13) can be expressed as,

$$J_n = -\sigma_n \nabla (V + \Pi_n + \frac{3k_B}{2q}T) + \nabla (\frac{\sigma_n k_B T}{q}) = -\sigma_n \nabla (V + S_n T + \frac{3k_B}{2q}T) + \nabla (\frac{\sigma_n k_B T}{q})$$
[14]

Hole current density, J_p , containing the drift and the diffusion components can also be derived using the same approach,

$$J_{n} = \underbrace{-\sigma_{n} \nabla \left(V + S_{n} T + \frac{3k_{B}}{2q} T\right)}_{J_{n,diffusion}} + \underbrace{\nabla \left(\frac{\sigma_{n} k_{B} T}{q}\right)}_{J_{n,diffusion}}$$
[15]

$$J_{p} = \underbrace{-\sigma_{p} \nabla \left(V + S_{p} T - \frac{3k_{B}}{2q} T\right)}_{J_{p,diffusion}} \underbrace{-\nabla \left(\frac{\sigma_{p} k_{B} T}{q}\right)}_{J_{p,diffusion}}$$
[16]

Equation (15) and (16) can be written using the following general form and expanded to compare with the previous model of J,

$$J_{n,p} = -\sigma_{n,p} \nabla \left(V + S_{n,p} T \pm \frac{3k_B}{2q} T \right) \pm \nabla \left(\frac{\sigma_{n,p} k_B T}{q} \right)$$
[17]

$$J_{n,p} = \underbrace{-\sigma_{n,p}\nabla V - \sigma_{n,p}S_{n,p}\nabla T}_{Previous\ model,\ equation\ (3)} \underbrace{-\sigma_{n,p}T\nabla S_{n,p} \mp \frac{1}{2}\frac{k_B}{q}\sigma_{n,p}\nabla T \pm \frac{k_B}{q}T\nabla\sigma_{n,p}}_{Additional\ terms\ in\ the\ new\ model}$$
[18]

In equation (17) and (18), for the terms following the (\pm) sign, + and - correspond to J_n and J_p respectively. Equation (18) clearly indicates the differences between the derived model in this work and earlier model as described by equation (3). The new model can capture the thermoelectric phenomena with more accuracy through the additional terms.

Here, it should be noted that carrier mobility is assumed to be a weak function of space and the Einstein relationship used to relate diffusion coefficient and carrier mobility assumes that diffusion coefficient is constant (not a function of space), $J_{n,diffusion} = qD_n^{Einstein}\frac{dn}{dx}$, instead of the more complete form $J_{n,diffusion} = q\frac{d(D_nn)}{dx}$ we have used in equations (7), (12)-(14). Thermally driven diffusion current, hence thermoelectric effects, cannot be captured if diffusion coefficient is assumed to be constant. An alternative approach to relate the diffusion coefficient to electrical conductivity would be through Wiedemann–Franz law (WFL), which relates the electronic component of thermal conductivity (k_e) to electrical conductivity as,

$$k_{\rho} = L\sigma T \tag{19}$$

where L is the Lorenz number. In absence of an external bias under a thermal gradient, the heat flux due to diffusing charge carriers (Fourier heat conduction) can be expressed in terms of k_e and the kinetic energy of the carriers similar to the derivation given above in equations (4)-(6),

Heat
$$Flux = \frac{d}{dx} (k_e T) = \frac{d}{dx} (\frac{3}{2} k_B T \frac{n}{2} v_{th}) \overline{l}$$
 [20]

Once again, assuming that \overline{l} is constant and can be included in the derivative,

$$k_e = \frac{3}{2} k_B \frac{n}{2} v_{th} \overline{l} = L \sigma T = L q n \mu_n T$$
 [21]

Hence,

$$v_{th} = \frac{4}{3} \frac{Lq\mu_n T}{k_B \bar{l}}$$
 [22]

Expressing $J_{n,diffusion}$ using a diffusion coefficient based on the WFL (D_n^{WFL}) and equating it to $J_{n,diffusion}$ derived in equations (4)-(6), we calculate a temperature dependent diffusion coefficient,

$$J_{n,diffusion} = \frac{d(qnD_n^{WFL})}{dx} = q \frac{1}{2} \left\{ \frac{d(nv_{th})}{dx} \right\} \overline{l}$$

$$qnD_n^{WFL} = \frac{1}{2} qnv_{th} \overline{l}$$

$$D_n^{WFL} = \frac{1}{2} v_{th} \overline{l} = \frac{2}{3} \frac{Lq\mu_n T}{k_B}$$
[23]

Comparing the two diffusion coefficients,

$$\frac{D_n^{WFL}}{D_n^{Einstein}} = \frac{\frac{2Lq\mu_n T}{3 k_B}}{\frac{\mu_n k_B T}{q}} = \frac{2}{3} \frac{Lq^2}{k_B^2} \approx \frac{2}{3} \times \frac{1.2 \times 10^{-8} V^2 K^{-2} \left(1.6 \times 10^{-19} C\right)^2}{\left(1.38 \times \frac{10^{-23} J}{K}\right)^2} = 1.08$$

Here we are using an experimental Lorenz number $(1.2 \times 10^{-8} \text{ V}^2\text{K}^{-2})$ reported for semiconductors with high Seebeck coefficients (21), similar to amorphous GST. The expressions we obtain using a diffusion coefficient based on the Einstein relation and the WFL have the same temperature dependence and their magnitudes are within 10% of each other. Hence, the diffusion coefficient we obtain using Einstein relation can be considered as a reasonable approximation and the diffusion currents calculated using $D_n^{Einstein}$ may be considered as the lower bound.

Results and Discussion

Thermoelectric heating/cooling along with Joule heating cause significantly varying temperature distribution profile inside the device for positive and negative polarity configurations leading to different crystal grain distributions within the phase change material. Thermoelectric heat transport is due to generation and recombination of electrons and holes as well as the kinetic energy absorbed or released by the transported free charge carriers (19) and is modeled as Thomson heat. The energy exchanges that can take place at material interfaces is defined as Peltier heat:

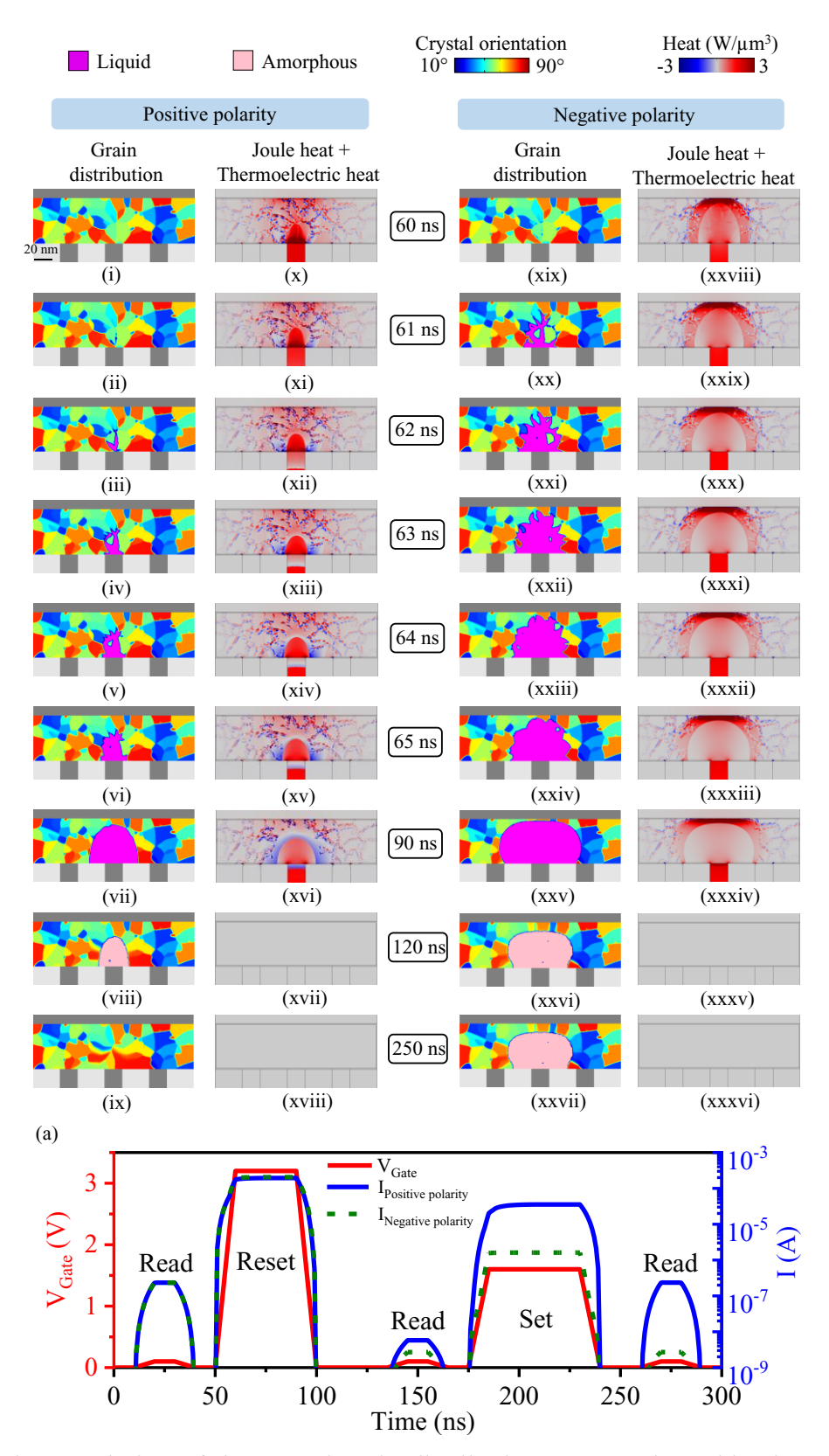


Figure 3. Time evolution of the crystal grain distribution maps and combined Joule and thermoelectric heat distribution profiles during the reset and set pulses for positive and negative polarity. V_{Gate} and current through the device, I during the sequential read-reset-read-set-read operations are shown in (a) where $V_{Reset} = 3.2V$, $V_{Set} = 1.6V$ and $V_{Read} = 0.1V$.

$$Q_{Thomson} = -\nabla. (JST)$$
 [24]

$$Q_{Peltier} = -J\Delta(ST)$$
 [25]

Figure 3 shows the time evolution of the grain arrangements inside the GST and the Joule and thermoelectric heats together in GST and TiN regions during the reset and set operations. For the same reset voltage amplitude, negative polarity results in faster melting and attains a larger amorphous area after quenching (over-reset). On the other hand, due to less net heating from Joule and thermoelectric effects, positive polarity results in a smaller amorphous area but optimized reset condition as the amorphous plug is only large enough to cover the heater for a high resistance state of the device. Consequently, the applied set voltage pulse can recrystallize the positive polarity device, whereas it is not sufficient to achieve electrical breakdown in the larger amorphous region of the negative polarity device.

Figure 4 shows the Joule, Thomson and Peltier heat distributions separately at the peak of the reset pulse. As the temperature rise is less in positive polarity (Figure 4g), GST remains more resistive which leads to higher Joule heating compared to the negative polarity. Thermoelectric heats change polarity (heating to cooling and vice-versa) with the reversal of current direction whereas the Joule effect always results in heating. Seebeck coefficient of GST is assumed to be zero for the liquid phase (Figure 5) so there is no Thomson heat within the molten region whereas the surrounding regions (liquid-crystal

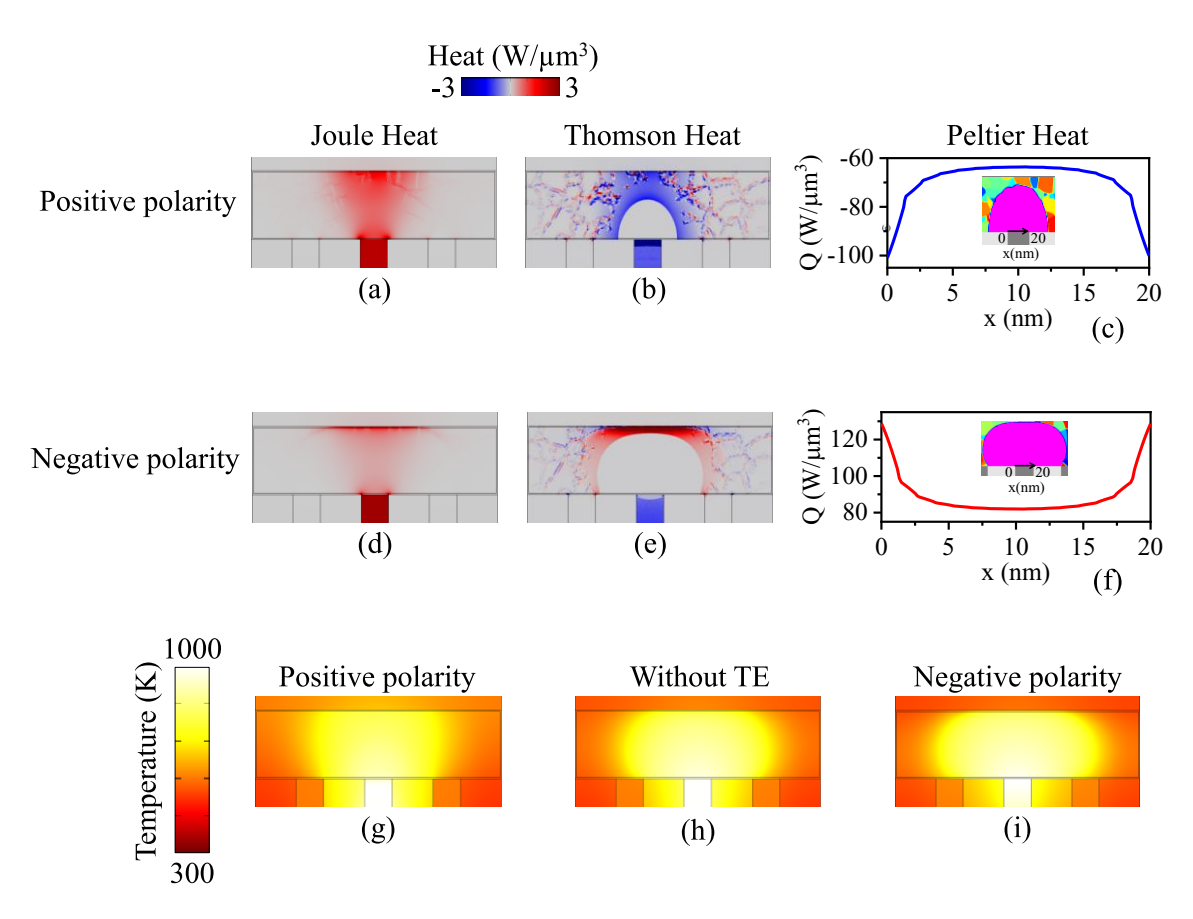


Figure 4. Heat dissipation at the peak of reset (Figure 3vii, xxv) due to Joule (a,d), Thomson (b,e) and Peltier (c,f) effects for positive and negative polarity and resultant temperature distribution profiles with TE effects (g,i) and without TE effects (h).

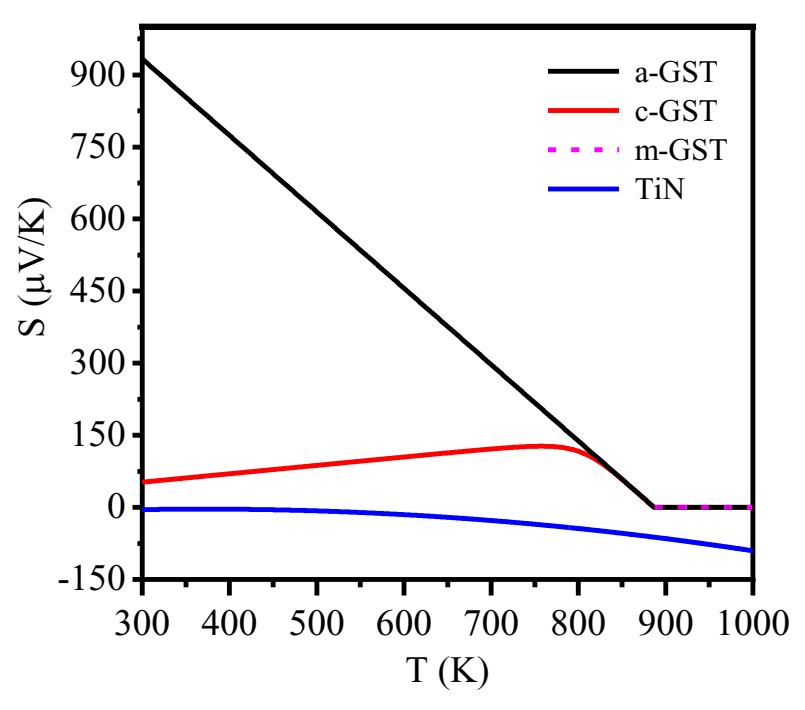


Figure 5. Seebeck coefficient of GST and TiN used in the simulation model based on the experimental results (22). a-, c- and m- stand for amorphous, crystalline and molten phase respectively.

interface) experience the greatest Thomson effect because of the largest gradients of Seebeck coefficient (Figure 4b,e). The grain boundaries also show pronounced Thomson effect because of the large gradients of electrical conductivity and Seebeck coefficient. It is also evident from the Figure 4(b,e) that Thomson cooling around the molten region of the positive polarity device hinders further melting and thus results in smaller amorphous area in comparison with the negative polarity case where Thomson heating surrounding the molten volume enhances the spread of the molten region. However, the model using J as the total current density does not capture heat transport by electrons and holes diffusing in the same direction which significantly enhance thermal conduction at the liquid-solid interfaces. This thermal conduction mechanism, generation of carriers in the melt - transport across the interface – recombination in the solid region (GTR) (19), is expected to dominate thermal transport at the solid-melt interfaces and can be captured by handling electron and hole currents (J_n, J_p) separately.

Peltier heat is absorbed (released) at the GST-heater boundary for positive (negative) polarity cells (Figure 4c,f) and is calculated assuming the heat at material junction is transmitted throughout a 1 nm thick volume. Peltier heat is larger than Joule and Thomson heat ($\sim 100~\text{W/}\mu\text{m}^3$ compared to $\sim 10\text{s}$ of W/ μm^3) for both polarities and this can be attributed to the larger difference in Seebeck coefficients between p-type GST and n-type TiN (Figure 5). Peltier heat has highest magnitude at the two corners of the heater in both positive and negative polarity because of current spreading.

We calculate the ratio of reset resistance to set resistance for different reset energy (Figure 6). Higher resistance ratio for the negative polarity at the same reset energy and initial set resistance indicates more melting followed by amorphization of the active region

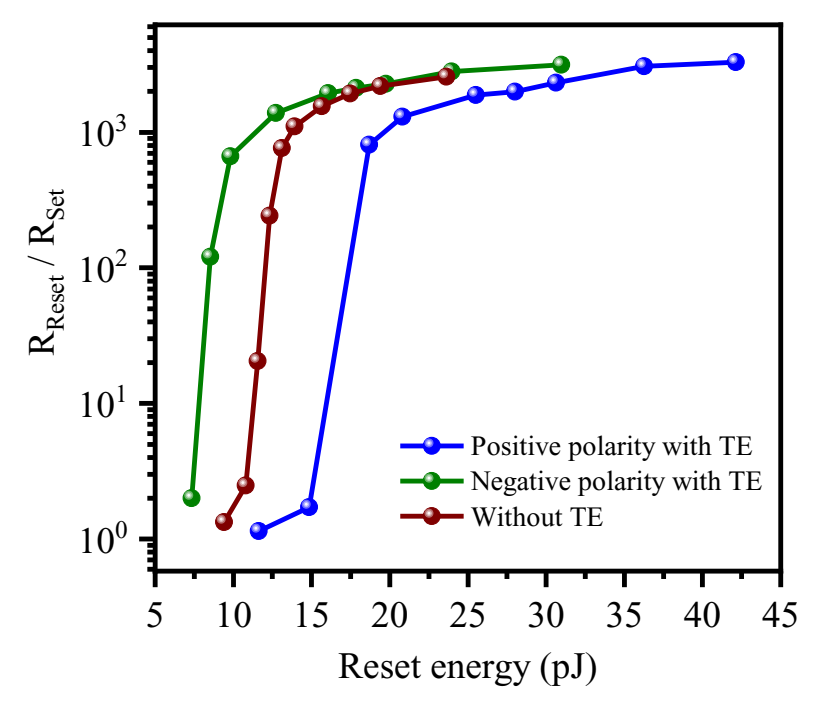


Figure 6. Reset state resistance to set state resistance ratio at different reset energy levels for positive and negative polarity with and without thermoelectric effects.

in negative polarity compared to the positive polarity. Quantitatively, negative polarity requires $\sim 2x$ less energy to achieve the successful reset state with sufficient resistance contrast ($\sim 10^2$). The simulations performed by removing the TE terms in equation (1), (15) and (16) show similar reset energy – resistance contrast relation as the negative polarity as the resistance contrast increases above 10^3 , while the results without TE terms are in between the two polarities for lower resistance contrasts.

Conclusions

We have investigated Joule heating and thermoelectric Thomson and Peltier effects on a mushroom PCM cell with a revised electro-thermal physics model that accounts for the effects of significant thermal gradients. Temperature and electric field dependent material parameters and thermal boundary resistances at the material interfaces have been used in the simulations to obtain the temperature gradient and corresponding phase changes resulting from current flow. Positive and negative polarity cells have been simulated to study the current polarity dependence of TE effects. Peltier heating at the GST-heater boundary and Thomson heating near the active region make the negative polarity cell more energy efficient, as it requires less current to make a set to reset transition. Though it is advantageous to have higher TE heating inside the mushroom and its interfaces for reduced power and energy consumption (negative polarity), TE cooling away from the mushroom interfaces is preferred for reduced thermal cross-talk and write-disturb on the neighbor cells (positive polarity).

Acknowledgements

M. T. B. Kashem acknowledges support from General Electric through a Graduate Fellowship for Innovation. This work is supported through US National Science Foundation (NSF) award # 1710468.

References

- 1. S. Raoux, G. W. Burr, M. J. Breitwisch, C. T. Rettner, Y. C. Chen, R. M. Shelby, M. Salinga, D. Krebs, S. H. Chen, H. L. Lung, and C. H. Lam, *IBM J. Res. Dev.*, **52**(4.5), 465 (2008).
- 2. Y. Zhang, S. Raoux, D. Krebs, L. E. Krupp, T. Topuria, M. A. Caldwell, D. J. Milliron, A. Kellock, P. M. Rice, J. L. Jordan-Sweet, and H. S. P. Wong, 2008. *J. Appl. Phys.*, **104**(7), 074312 (2008).
- 3. G. W. Burr, M. J. Brightsky, A. Sebastian, H. Y. Cheng, J. Y. Wu, S. Kim, N. E. Sosa, N. Papandreou, H. L. Lung, H. Pozidis, and E. Eleftheriou, *IEEE J. Em. Sel. Top. C.*, **6**(2), 146 (2016).
 - 4. S. Lai and T. Lowery, *IEDM Tech. Dig.*, 803 (2001).
- 5. A. Faraclas, G. Bakan, F. Dirisaglik, N. E. Williams, A. Gokirmak, and H. Silva, *IEEE Trans. Electron Dev.*, **61**(2), 372 (2014).
- 6. D. T. Castro, L. Goux, G. A. M. Hurkx, K. Attenborough, R. Delhougne, J. Lisoni, F. J. Jedema, R. A. Wolters, D. J. Gravesteijn, M. A. Verheijen, and M. Kaiser, *IEEE Int. El. Devices Meet.* 315 (2007).
- 7. K. L. Grosse, F. Xiong, S. Hong, W. P. King, and E. Pop, *Appl. Phys. Lett.*, **102**(19), 193503 (2013).
 - 8. X. Lian, J. Fu, Z. Gao, and L. Wang, *IEEE Trans. Electron Dev.*, **68**(12), 6139 (2021).
- 9. D. S. Suh, C. Kim, K. H. Kim, Y. S. Kang, T. Y. Lee, Y. Khang, T. S. Park, Y. G. Yoon, J. Im, and J. Ihm, *Appl. Phys. Lett.*, **96**(12), 123115 (2010).
 - 10. J. Lee, M. Asheghi, and K. E. Goodson, *Nanotechnology*, **23**(20), 205201 (2012).
- 11. J. Bahl, B. Rajendran, and B. Muralidharan, *IEEE Trans. Electron Dev.*, **62**(12), 4015 (2015).
- 12. "COMSOL Multiphysics Reference Manual, version 5.5", COMSOL, Inc, www.comsol.com.
 - 13. Z. Woods, and A. Gokirmak, *IEEE Trans. Electron Dev.*, **64**(11), 4466 (2017).
- 14. Z. Woods, J. Scoggin, A. Cywar, and A. Gokirmak, *IEEE Trans. Electron Dev.*, **64**(11), 4472 (2017).
- 15. J. Scoggin, R. S. Khan, H. Silva, and A. Gokirmak, *Appl. Phys. Lett.*, **112**(19), 193502 (2018).
- 16. J. Scoggin, Z. Woods, H. Silva, and A. Gokirmak, *Appl. Phys. Lett.*, **114**(4), 043502 (2019).
- 17. R. S. Khan, N. H. Kan'an, J. Scoggin, H. Silva, and A. Gokirmak, *Mat. Sci. Semicon. Proc.*, **134**, 106042 (2021)
- 18. N. Ciocchini, M. Laudato, A. Leone, P. Fantini, A. L. Lacaita, and D. Ielmini, *IEEE Trans. Electron Dev.*, **62**(10), 3264 (2015).
 - 19. G. Bakan, N. Khan, H. Silva, and A. Gokirmak, Sci. Rep., 3(1), 1 (2013).
- 20. B. G. Streetman, and S. Banerjee, *Solid State Electronic Devices*, p. 140, Upper Saddle River: Pearson/Prentice Hall, New Jersey (2013).

- 21. H. S. Kim, Z. M. Gibbs, Y. Tang, H. Wang, and G. J. Snyder, *APL Mater.*, **3**(4), 041506 (2015).
- 22. L. Adnane, F. Dirisaglik, A. Cywar, K. Cil, Y. Zhu, C. Lam, A. F. M. Anwar, A. Gokirmak, and H. Silva, *J. Appl. Phys.*, **122**(12), 125104 (2017).